Electrochemical Dy-Alloying Behaviors of Ni-Based Alloys in Molten LiF–CaF2–DyF3: Effects of Constituent Elements

AUTHOR(S):

Yasuda, Kouji; Enomoto, Terumichi; Watanabe, Yusaku; Oishi, Tetsuo; Nohira, Toshiyuki

CITATION:

Yasuda, Kouji ...[et al]. Electrochemical Dy-Alloying Behaviors of Ni-Based Alloys in Molten LiF–CaF2–DyF3: Effects of Constituent Elements. MATERIALS TRANSACTIONS 2020, 61(12): 2329-2335

ISSUE DATE:

2020-12

URL:

http://hdl.handle.net/2433/263277

Materials Transactions, Vol. 61, No. 12 (2020) pp. 2329 to 2335

Electrochemical Dy-Alloying Behaviors of Ni-Based Alloys in Molten LiF–CaF_2–DyF_3: Effects of Constituent Elements

Kouji Yasuda[1,2,*1], Terumichi Enomoto[3], Yusaku Watanabe[3,*2], Tetsuo Oishi[4] and Toshiyuki Nohira[3,*3]

[1]*Agency for Health, Safety and Environment, Kyoto University, Kyoto 606-8501, Japan*
[2]*Department of Fundamental Energy Science, Graduate School of Energy Science, Kyoto University, Kyoto 606-8501, Japan*
[3]*Institute of Advanced Energy, Kyoto University, Uji 611-0011, Japan*
[4]*Global Zero Emission Research Center, National Institute of Advanced Industrial Science and Technology (AIST), Tsukuba 305-8569, Japan*

The electrochemical Dy-alloying behaviors of Ni–Cr and Ni–Mo alloys were compared with those of Ni–Cr–Mo alloy and pure Ni in a molten LiF–CaF_2–DyF_3 (0.30 mol%) system at 1123 K. The effects of chromium and molybdenum as constituent elements of the Ni-based alloys were investigated. Cyclic voltammetry and open-circuit potentiometry indicated the formations of Dy–Ni alloys for all the Ni-based electrodes, as well as for the pure Ni electrode. XRD analysis confirmed the formation of $DyNi_2$ and $DyNi_3$ phases for all the electrodes electrolyzed at 0.20 V (vs. Li^+/Li) for 60 min. SEM/TEM-EDX analysis of the sample prepared from Ni–Cr–Mo alloy revealed that the Dy-alloyed layer consists of Cr-rich Cr–Mo and Mo-rich Mo–Cr phases, as well as a Dy–Ni(–Fe) matrix phase. The shear stress measurements of the Dy-alloyed samples showed that the Ni–Cr–Mo alloy is the most suitable substrate to improve mechanical strength, which is explained by precipitation strengthening by both the Cr–Mo and Mo–Cr phases. [doi:10.2320/matertrans.MT-M2020200]

(Received June 18, 2020; Accepted August 31, 2020; Published October 23, 2020)

Keywords: *rare earth, molten salt, recycling, electrochemistry, fluoride, dysprosium*

1. Introduction

Due to the widespread use of hybrid electric vehicles (HEVs) and electric vehicles (EVs), there has been an increase in the production volumes of Nd–Fe–B magnets, which are used for constructing high-performance motors. The addition of Dy to Nd–Fe–B magnets is necessary to maintain its strong magnetic properties even at high operating temperatures above 473 K. The addition of Dy is also necessary for the Nd–Fe–B magnets used for wind power generators and air conditioners.

With the increasing demand and unstable supply of rare earth (RE) elements due to the uneven distribution of their resources, i.e., China dominated 63% of the global RE-mine production in 2019,[1)] recycling RE elements has become a necessary option to manage demand. However, only in-process recycling of materials generated during the cutting and forming stages is presently carried out in magnet plants. The recycling of discarded commercial products is rarely conducted except for large ones used in magnetic resonance imaging (MRI). Recycling reduces the impact of mining and the accumulation of radioactive waste on the environment, thus protecting the environment. Therefore, the development of new and efficient recycling methods for RE metals from magnet scraps is strongly required. Several pyrometallurgical processes, such as extraction into molten metal,[2,3)] molten salts,[4,5)] and molten slags;[6,7)] electrolysis in ionic liquids and molten salts;[8,9)] and selective vaporization[10)] have been proposed and investigated as new recycling methods.

Recently, we proposed a separation and recovery process for RE metals from magnet scraps using molten salt and an alloy diaphragm.[9,11–19)] We confirmed the selective and electrochemical formation of RE–Ni alloys (RE = Nd, Pr, and Dy) in molten LiF–CaF_2–REF_3 salts at 1123 K[12–14,18)] and molten NaCl–KCl–$RECl_3$ salts at 973 K,[15–18)] which indicated that the process has a good RE separation ability in a certain potential range. However, the brittleness and low durability of RE–Ni alloys affects their long-term use. To develop a more durable alloy diaphragm, we selected Ni-based alloys such as Inconel 600 and Hastelloy C-276 as candidates for base materials.[19)] We confirmed the presence of aggregated phases of Cr and Mo in Dy–Ni alloy layer in molten LiF–CaF_2–DyF_3 salts at 1123 K, wherein, the aggregation degree of Mo was lower than that of Cr. The presence of the aggregated phases in the alloy layer suggested an improvement in the mechanical strength due to precipitation strengthening, however, the actual mechanical strength was not measured.

In our previous study, we could not distinguish the individual effect of Cr and Mo on the electrochemical behavior of Hastelloy C-276, as it contains Cr, Mo, and Ni as constituent elements. In the present study, we investigated the effects of constituent elements on the electrochemical Dy-alloying behaviors of Ni-based alloys in molten LiF–CaF_2–DyF_3 (0.30 mol%) system at 1123 K. Furthermore, we investigated and compared the Dy-alloying behaviors of Ni–Cr and Ni–Mo alloys. The formed Dy-alloys were studied by X-ray diffraction (XRD), cross-sectional scanning electron microscopy (SEM), transmission electron microscopy (TEM), and energy-dispersive X-ray spectrometry (EDX). The results of Ni–Cr–Mo, Ni–Cr, Ni–Mo alloys, and pure Ni were compared. Finally, the effect of the constituent elements on the mechanical strength was evaluated by measuring the shear stress of the formed alloy samples.

2. Experimental Procedure

The details of the experimental setup and procedure have been reported in our previous study.[14,19)] LiF (Fuji Film

*[1]Present address: Department of Materials Science and Engineering, Graduate School of Engineering, Kyoto University, Kyoto 606-8501, Japan
*[2]Graduate Student, Kyoto University
*[3]Corresponding author, E-mail: nohira.toshiyuki.8r@kyoto-u.ac.jp

Wako Pure Chemical Corp., >98%) and CaF_2 (Kojundo Chemical Laboratory Co., Ltd., 99.9%) were mixed to an eutectic composition ($LiF:CaF_2 = 80.5:19.5$ mol%), and 300 g of the eutectic mixture was loaded into a graphite crucible (Toyo Tanso Co., Ltd., IG-110, i.d. 90 mm × height 120 mm). The eutectic mixture in the crucible was dried under a vacuum at 453 K for 72 h. The crucible was then placed at the bottom of a stainless-steel vessel in an air-tight Kanthal container and further dried under a vacuum at 773 K for 24 h. The electrochemical measurements were conducted in a glove box under Ar atmosphere at 1123 K. Powdery DyF_3 (Kojundo Chemical Laboratory Co., Ltd., 99.9%) was added directly into the melts. Three types of electrodes: wire (1.0 mm in diameter), plate (10-mm width × 10-mm length × 0.1-mm thickness), and flag (diameter: 3.0 mm, thickness: 0.1 mm, lead wire diameter: 0.1 mm)[20] were used as the working electrodes. Hastelloy C-276® (Nilaco Corp.), Nichrome® (Nilaco Corp.), an alloy equivalent to Hastelloy B-2® (Kouei Co. Ltd.), Ni (Nilaco Corp., >99%), and Mo (Nilaco Corp., 99.95%) were used as the materials for the working electrodes. Table 1 lists the compositions of the alloys reported in the catalogue. All the materials contain Ni as the main constituent element except the pure Mo metal. Hastelloy C-276®, Nichrome®, and Hastelloy B-2® will be regarded and hereafter as Ni–Cr–Mo, Ni–Cr, and Ni–Mo alloys, respectively. Minor elements contained in Hastelloy C-276, such as iron and tungsten, may also influence its Dy-alloying behavior, however, their effect was neglected and only the major constituents were studied. A Pt wire (Tanaka Kikinzoku Kogyo Corp., 99.95%, diameter: 1 mm) immersed in the bulk melt was used as a quasi-reference electrode and its potential was calibrated with reference to the potential of the Li^+/Li dynamic reference electrode, which was prepared by electrodepositing Li metal on a Mo electrode. All the potentials in this paper are reported with reference to the Li^+/Li potential. The counter electrode was a glassy carbon rod (Tokai Carbon Co., Ltd., diameter: 3.0 mm, immersion depth: 10 mm). An electrochemical measurement system (Hokuto Denko Corp., HZ-7000) connected to a personal computer was used for the measurement. Alloy samples were prepared by the potentiostatic electrolysis of the plate-type electrodes. Cross-sections of the alloy samples were characterized by SEM (Keyence Corp., VE-8800), field-emission scanning electron microscopy (FE-SEM; Hitachi Corp., SU-8020), and TEM (JEOL Ltd., JEM-2100PLUS). For the SEM and FE-SEM analysis, the samples were embedded in resin, polished with emery paper (#320 and #600) and polycrystalline diamond suspension (#3, 9 μm), and then coated with Au by an ion sputtering apparatus (Hitachi, Ltd., E-1010) to give conductivity. The TEM samples were prepared by focus ion beam (FIB) using Ga ions. The compositions of the samples were analyzed by EDX (HORIBA Ltd., X-Max^{N}80 and JEOL Ltd., JEM-2100). After the SEM analysis, fluoride salts covering the alloy samples were removed by a hand grinder (Kiso Power Tool Mfg. Co., Ltd., No. 28525-S). Subsequently, the alloy phases were identified by XRD (Rigaku Corp., Ultima IV) using Cu-$K\alpha$ radiation ($\lambda = 0.15418$ nm) at 40 kV and 40 mA. The mechanical strength of the alloy samples was evaluated by measuring the shear stress. To measure the shear stress, a shear punch test was performed for an alloy sample (10-mm width × 10-mm length × 0.17-mm thickness) sandwiched between two acrylic plates at room temperature using a stainless steel punch with a diameter of 2 mm attached to a load cell (IMADA, ZTS-500N). The punch feed rate was manually controlled at around 0.1 mm s^{-1}. The shear stress was measured at several different points, and the average value was calculated.

3. Results and Discussions

3.1 Cyclic voltammetry

Figure 1 shows the cyclic voltammograms for (a) Ni–Cr–Mo,[19] (b) Ni–Cr, and (c) Ni–Mo flag electrodes in a molten $LiF–CaF_2–DyF_3$ (0.30 mol%) system at 1123 K. The voltammogram for Ni flag electrode is also given for reference. For Ni–Cr–Mo alloy, as reported in Ref. 19), cathodic currents (A) are observed from 0.7 V (vs. Li^+/Li) in the negative scan direction, which corresponds to the formation of Dy–Ni alloys.[19] From 0.4 V, cathodic currents (B) and (C) flow consecutively in the negative scan direction, this is due to the formation of Dy–Ni alloys with higher Dy concentrations.[19] The phase diagram of the Dy–Ni system[21] indicates the existence of nine intermetallic compounds: Dy_3Ni_2, DyNi, $DyNi_2$, $DyNi_3$, Dy_2Ni_7, $DyNi_4$, Dy_4Ni_{17}, $DyNi_5$, and Dy_2Ni_{17} at 1123 K, as well as the existence of a liquid alloy with a Dy-rich composition. In comparison to the voltammogram for the Ni electrode, that for the Ni–Cr–Mo electrode had smaller cathodic currents and larger overpotentials. This is because the agglomerated Cr–Fe–Mo phase retards Dy diffusion in the alloy layer.[19] After the reversal of the scanning direction, four anodic peaks

Table 1 Compositions of the Ni–Cr–Mo, Ni–Cr, and Ni–Mo alloys used for the experiments.

	Composition of element i, w_i / (wt%)					Note
	Ni	Cr	Mo	Fe	W	
Ni–Cr–Mo	> 57	16	17	4–7	3–4	Hastelloy C-276®
Ni–Cr	> 77	19-21	—	—	—	Nichrome®
Ni–Mo	Bal.	0.7	28.2	1.7	—	An alloy equivalent to Hastelloy B-2®

(a) Ni–Cr–Mo alloy

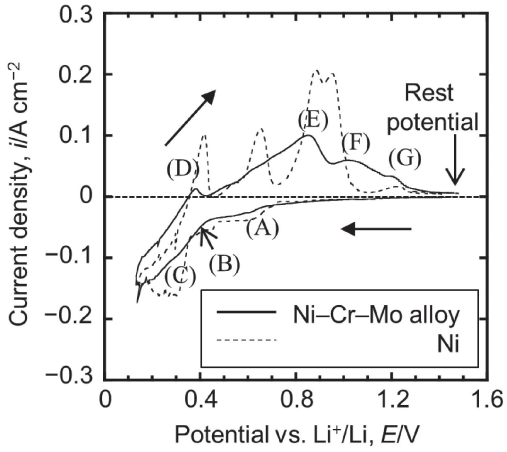

(b) Ni–Cr alloy

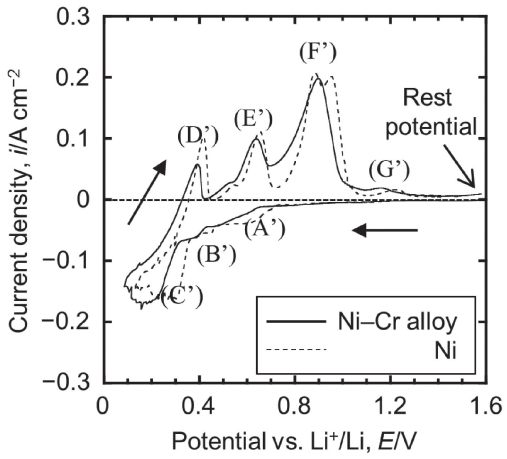

(c) Ni–Mo alloy

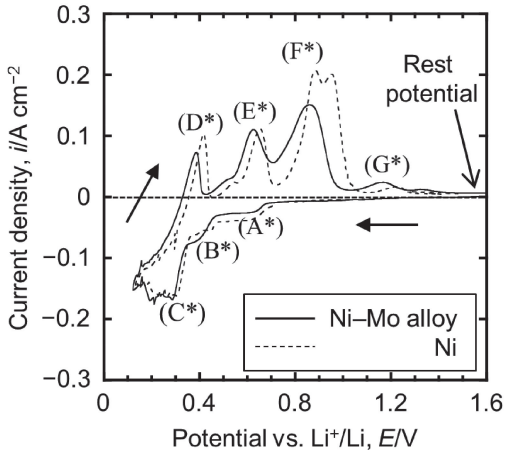

Fig. 1 Cyclic voltammograms for (a) Ni–Cr–Mo,[19] (b) Ni–Cr, and (c) Ni–Mo flag electrodes in molten LiF–CaF_2–DyF_3 (0.30 mol%) at 1123 K. The voltammogram for the Ni flag electrode is also given for comparison. Scan rate = 50 mV s^{-1}.

corresponding to the dissolutions of Dy from different Dy–Ni alloy phases are observed. The blunt anodic peaks of the Dy–Ni alloy compared with those of the pure Ni is due to the slow Dy diffusion in the alloy layer.[19]

General features of the voltammograms for (b) Ni–Cr and (c) Ni–Mo alloys are similar to that for (a) Ni–Cr–Mo alloy. However, the Ni–Mo alloy has smaller overvoltage for the formation of Dy–Ni alloys in comparison to the other alloys. This suggest that the Mo component in the Ni–Mo alloy has little influence on the alloying overvoltage and the Dy diffusivity. After the reversal of the scanning direction for (b) and (c), four anodic peaks are observed more clearly in comparison to that of (a), suggesting faster dealloying rates for Ni–Cr and Ni–Mo alloys than for Ni–Cr–Mo alloy.

3.2 Open-circuit potentiometry

Open-circuit potentiometry was conducted for Ni–Cr–Mo, Ni–Cr, Ni wire electrodes and a Ni–Mo plate electrode after galvanostatic electrolysis at −0.3 A cm^{-2} for 100 s in a molten LiF–CaF_2–DyF_3 (0.3 mol%) system at 1123 K. Figure 2(a) compares the open-circuit potentiograms of Ni–Cr–Mo and Ni wire electrodes.[19] The electrode potential is seen to shift in the positive direction with time, this is because the Dy concentration at the electrode surface decreases as Dy atoms diffuse toward the center of the electrode. Potential plateaus for the Ni–Cr–Mo alloy are observed at 0.41, 0.58, and 0.76 V, which correspond to the coexisting $DyNi_2$/$DyNi_3$, $DyNi_3$/$DyNi_5$, and $DyNi_5$/Ni equilibria phases (eq. (1)), respectively.[19]

$$Dy_xNi + (y - x)Dy(III) + 3(y - x)e^- \leftrightarrows Dy_yNi \quad (1)$$

Figures 2(b) and (c) show the open-circuit potentiograms for the Ni–Cr and Ni–Mo alloys, respectively. For comparison, the potentiograms of the Ni electrode are also plotted. Although the scales of the time axes are slightly different for (a), (b), and (c), the potentiograms show similar potential plateaus as those observed for the Ni electrode. However, new potential plateaus are observed for (c) at 0.65 V and 0.73 V, for unknown reasons. Table 2 summarizes the observed plateau potentials for Ni–Cr–Mo, Ni–Cr, Ni–Mo alloys, and Ni. Since similar values are observed, the observed potential plateaus reasonably correspond to the coexisting states of Dy–Ni alloys expressed as reaction (1) for all cases.

3.3 Preparation of Dy alloys and their characterization

In our previous study, we confirmed that the deposition of Dy metal on a Mo electrode and the formation of $DyNi_2$ from a Ni substrate occurs at 0.16 V and 0.20 V in a molten LiF–CaF_2–DyF_3 (0.3 mol%) system at 1123 K, respectively.[14] Therefore, the electrolysis condition for the preparation of Dy-alloyed samples from Ni–Cr–Mo, Ni–Cr, and Ni–Mo plate electrodes was set at 0.20 V for 60 min. For all the electrodes, the cathodic current density gradually decreased from *ca.* 150 mA cm^{-2} to *ca.* 50 mA cm^{-2}. Figure 3(a) shows the cross-sectional SEM image of the sample prepared from the Ni–Cr–Mo alloy. From the SEM image, it is found that the thickness of the sample increased from 100 μm to 170 μm, which is due to volume expansion by alloying. In accordance with an EDX result indicating the atomic ratio of Dy/Ni ≈ 2.2 in the alloy layer, the XRD pattern of the Ni–Cr–Mo alloy in Fig. 4(a) confirms the formation of a $DyNi_2$ phase accompanying a $DyNi_3$ phase. Figures 3(b) and (c) show the cross-sectional SEM images of the samples

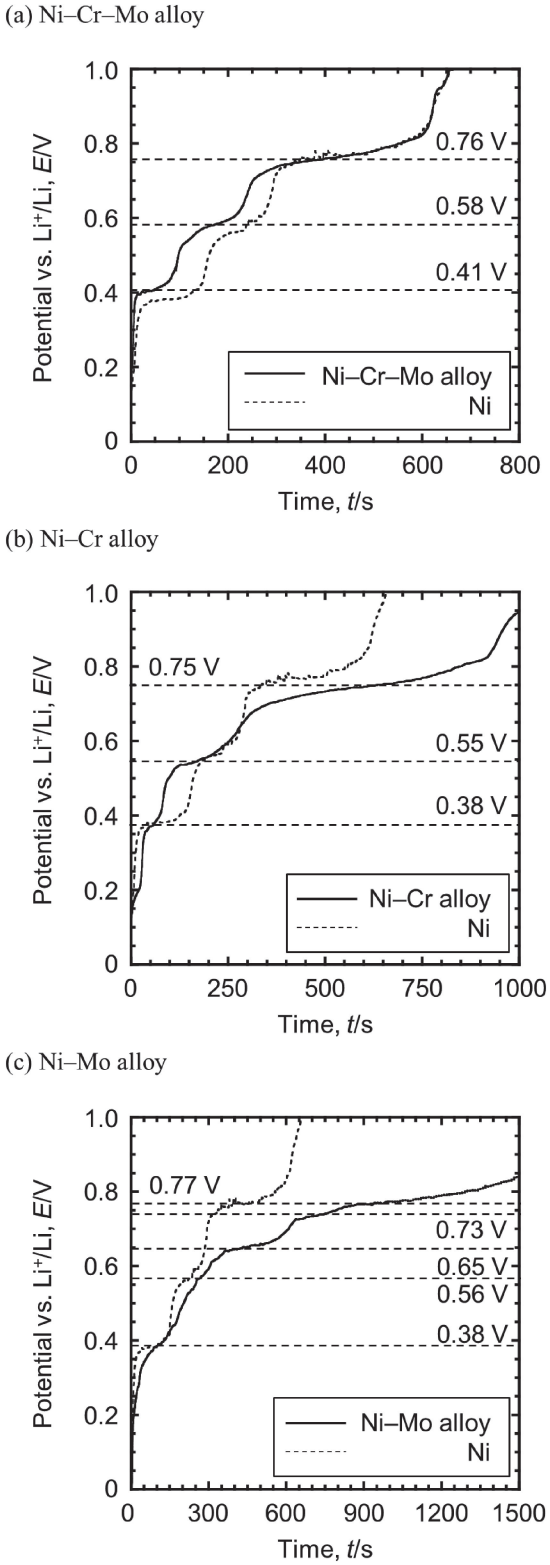

Fig. 2 Open-circuit potentiograms for (a) Ni–Cr–Mo wire,[19] (b) Ni–Cr wire, and (c) Ni–Mo plate electrodes after galvanostatic electrolysis at $-0.3\,A\,cm^{-2}$ for 100 s in molten LiF–CaF_2–DyF_3 (0.30 mol%) at 1123 K. The potentiogram for the Ni wire electrode is also given for comparison.

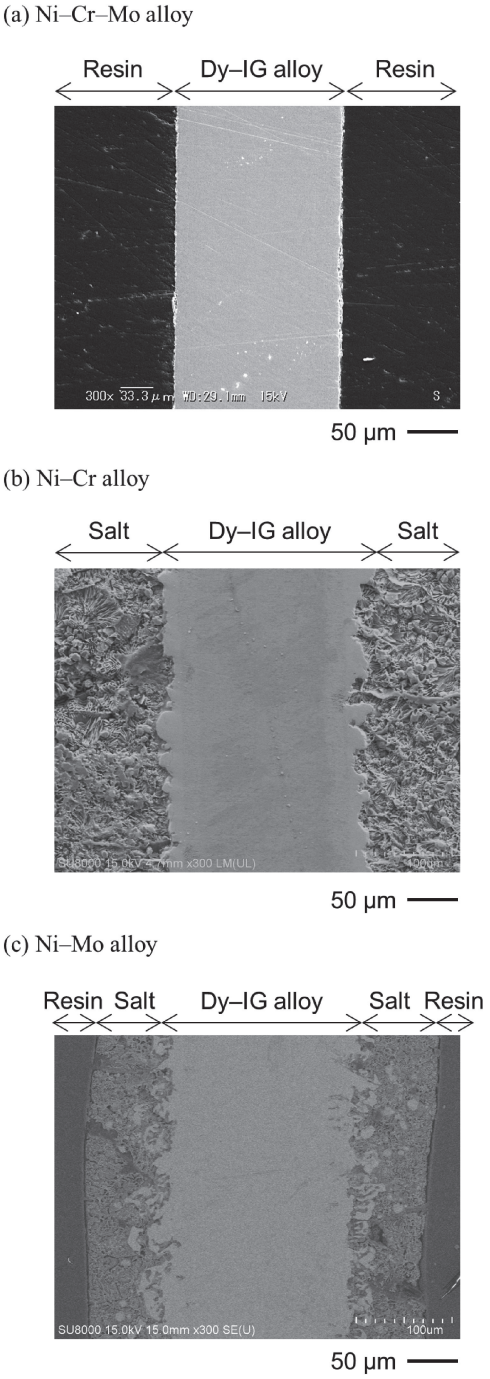

Fig. 3 Cross-sectional SEM images of the samples prepared by the potentiostatic electrolysis of (a) Ni–Cr–Mo, (b) Ni–Cr, and (c) Ni–Mo plate electrodes at 0.20 V for 60 min in molten LiF–CaF_2–DyF_3 (0.30 mol%) at 1123 K.

prepared from Ni–Cr and Ni–Mo plates, respectively. In both samples, the thickness of the alloyed sample was approximately 170 μm. This agrees with the theoretical volume expansion for the formation of $DyNi_2$, which is calculated on the assumption that the constituent Ni forms $DyNi_2$, while other constituents do not contribute to volume expansion. Figures 4(b) and (c) show the XRD patterns of the Ni–Cr and Ni–Mo samples, respectively. For comparison, the XRD pattern of the sample prepared from the Ni plate is also plotted in Fig. 4(d). For all cases, the formation of a $DyNi_2$ phase is confirmed.

The above samples were analyzed by cross-sectional SEM-EDX mapping at high magnification to obtain the distribution of the elements as shown in Fig. 5. The object elements are Dy, Ni, Cr, Fe, and Mo. Dark-spot patterns are observed in the SEM image of the Ni–Cr–Mo alloy (a), which indicates a

Table 2 Equilibrium reactions and corresponding potentials of the Dy–Ni alloys from Ni–Cr–Mo wire, Ni–Cr wire, and Ni–Mo plate electrodes after galvanostatic electrolysis at $-0.3\ A\ cm^{-2}$ for 100 s in molten LiF–CaF_2–DyF_3 (0.30 mol%) at 1123 K. The potentials of Ni wire electrode are also given for comparison.[14)]

Equilibrium reaction	Potential vs. Li^+/Li, E/V			
	Ni–Cr–Mo [19)]	Ni–Cr	Ni–Mo	Nickel [14)]
(1) $5\ Ni + Dy(III) + 3\ e^- \rightleftarrows DyNi_5$	0.76	0.75	0.77	0.77
(2) $3/2\ DyNi_5 + Dy(III) + 3\ e^- \rightleftarrows 5/2\ DyNi_3$	0.58	0.55	0.56	0.57
(3) $2\ DyNi_3 + Dy(III) + 3\ e^- \rightleftarrows 3\ DyNi_2$	0.41	0.38	0.38	0.38

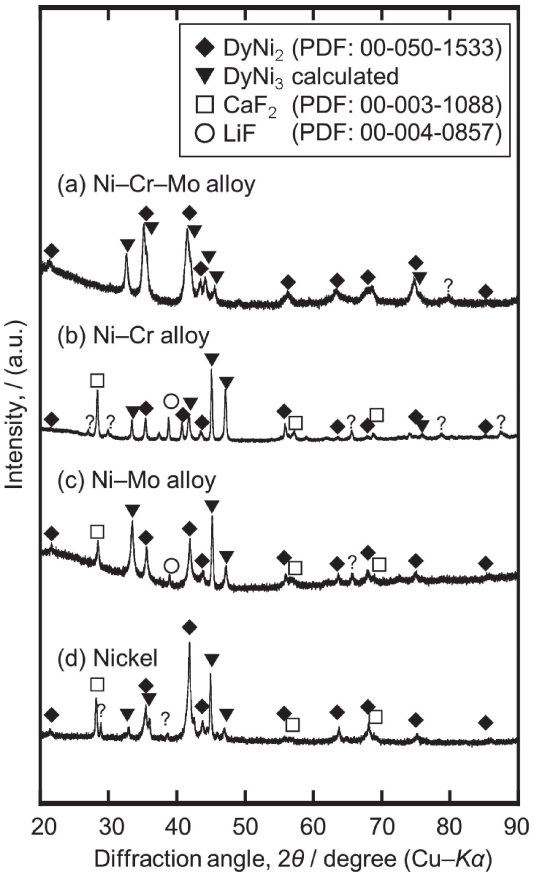

Fig. 4 XRD patterns of the samples prepared by the potentiostatic electrolysis of (a) Ni–Cr–Mo, (b) Ni–Cr, (c) Ni–Mo, and (d) Ni plate electrodes at 0.20 V for 60 min in molten LiF–CaF_2–DyF_3 (0.30 mol%) at 1123 K.

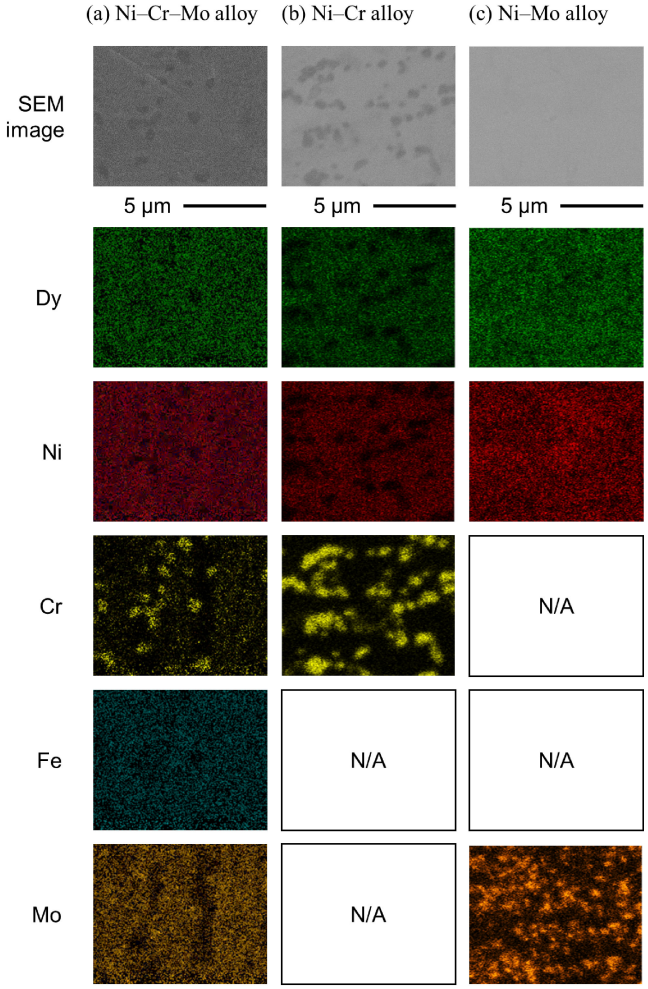

Fig. 5 Cross-sectional SEM and EDX mapping images of the samples obtained by the potentiostatic electrolysis of (a) Ni–Cr–Mo,[19)] (b) Ni–Cr, and (c) Ni–Mo plate electrodes at 0.20 V for 60 min in molten LiF–CaF_2–DyF_3 (0.30 mol%) at 1123 K.

high concentration of Cr. The precipitation of the agglomerated Cr phase occurred because there is no existence of a Cr–Dy alloy phase.[22)] The Cr precipitation is explained by the reported phase equilibria in the Ni–Cr–Mo system at 1123 K shown in Fig. 6.[23)] When Ni component in the Ni–Cr–Mo alloy forms an alloy with Dy, the nominal composition of the precipitated phase changes along the blue arrow toward the final composition (A), Mo:Cr = 52:48 at% excluding other elements. Since the Cr–Mo system shows a solid miscibility gap at a critical temperature of 1153 K at ~39 at% Mo,[24)] the (B) Cr-rich Cr–Mo and (C) Mo-rich Mo–Cr phases coexist at the nominal composition (A) at 1123 K. From EDX mapping images for Cr and Mo in Fig. 5(a), the coexistence of Mo is confirmed at the dark-spot patterns of Cr-rich phase. The SEM image of the (b) Ni–Cr alloy shows dark-spot patterns with a diameter of 0.2–1 μm, of which the distribution of the dark-spot patterns coincides with that of Cr. It was difficult to determine the accurate composition at the dark-spot patterns due to the limited spatial resolution of the SEM/EDX equipment. The EDX mapping of Mo in (c) Ni–Mo alloy shows the precipitation

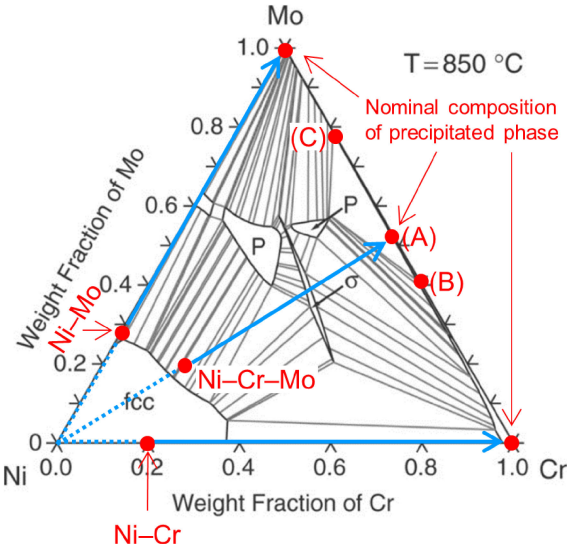

Fig. 6 Estimated phase change drawn in the calculated isothermal sections of the Ni–Cr–Mo phase diagram at 1123 K.[23)]

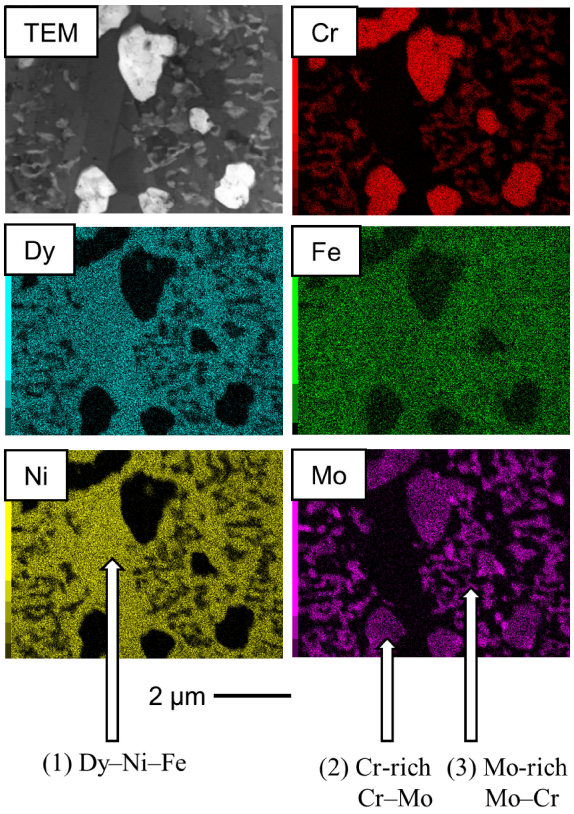

Fig. 7 Cross-sectional TEM and EDS mapping images of the sample obtained by the potentiostatic electrolysis of the Ni–Cr–Mo plate electrode at 0.20 V for 120 min in molten LiF–CaF_2–DyF_3 (0.30 mol%) at 1123 K.

and agglomeration of Mo with a diameter of 50–100 nm, which cannot be identified in the SEM image.

TEM-EDX mapping of the sample from Ni–Cr–Mo alloy carried out to obtain a more detailed distribution of the elements is shown in Fig. 7. The object elements are Dy, Ni, Cr, Fe, and Mo. The precipitated and agglomerated phase appears as bright-spot patterns in the TEM image. Because the spatial resolution of TEM-EDX is higher than that of SEM-EDX, additional information is obtained. The first point on the image corresponds the distribution of Fe, the TEM/EDX mapping clearly indicates that Fe is contained in the Dy–Ni phase. The average composition of the Dy–Ni–Fe matrix phase (point (1)) is determined to be 26.7 at% Dy, 68.8 at% Ni, 3.1 at% Fe, and 1.4 at% others. Such distribution of Fe is explained by the high affinity of Dy, Ni, and Fe; as all the binary systems: Dy–Ni, Dy–Fe, and Ni–Fe, have several alloy phases.[21,22,25)] The second point corresponds to the precipitated phase of Cr and Mo. The TEM/EDX mappings of Cr and Mo show that these two elements distribute in two different phases: Cr-rich Cr–Mo phase with a diameter of 0.2–1 μm (point (2)) and Mo-rich Mo–Cr phase with a diameter of 50–100 nm (point (3)). The average composition of the (2) Cr-rich Cr–Mo phase is 79.4 at% Cr, 13.5 at% Mo, and 7.1 at% others. While the average composition of the (3) Mo-rich Mo–Cr phase is 44.2 at% Cr, 29.2 at% Mo, and 26.6 at% others. The average composition of the Ni–Cr–Mo alloy (Hastelloy C-276) measured by EDX before the electrolysis was 19.4 at% Cr, 6.0 at% Fe, 61.2 at% Ni, 12.4 at% Mo, and 1.0 at% W. Thus, the atomic ratio of Cr:Mo is 61:39 in this system. As explained in the previous paragraph using Fig. 6, the phase separation into the (2) Cr-rich Cr–Mo phase and (3) Mo-rich Mo–Cr phase at 1123 K is consistent with the phase diagrams of the Ni–Cr–Mo[23)] and Cr–Mo[24)] systems.

Since the presence of the precipitated and agglomerated phases in the alloy layer is expected to reduce the brittleness of RE–Ni alloys, the mechanical strength was evaluated by measuring the shear stress for each of the Dy-alloyed sample. Figure 8 compares the shear stresses of the Dy-alloyed plates prepared from Ni–Cr–Mo, Ni–Cr, and Ni–Mo alloys at 0.20 V for 60 min. Because the existence of unalloyed part in the sample causes significant positive error in the measurements, the cross section of the samples was observed by SEM to confirm if the whole sample was alloyed or not. Error bars represent the standard deviations. For comparison, the result of Dy-alloyed samples prepared from Ni plates is also given. For these samples, the electrolysis condition was 0.20 V for 25–40 min in the same molten salt. The Dy–Ni alloy prepared from pure Ni plate was very brittle with a shear stress of only 15.6 N mm^{-2}. The shear stress values for Ni–Cr–Mo, Ni–Cr, and Ni–Mo alloys are 75.8, 16.6, and 10.1 N mm^{-2}, respectively. These data clearly show that the improvement in the mechanical strength of the alloys by precipitation strengthening was achieved only in the Ni–Cr–Mo alloys. It is suggested that both the Cr-rich Cr–Mo phase and the Mo-rich Mo–Cr phase play important roles in achieving the high reinforcement. These results are beneficial in selecting the constituent elements of the alloy diaphragm which will have high Dy diffusivity and high mechanical strength.

4. Conclusion

The electrochemical Dy-alloying behavior of Ni–Cr–Mo, Ni–Cr, and Ni–Mo electrodes were investigated and compared in a molten LiF–CaF_2–DyF_3 (0.30 mol%) system at 1123 K. The cyclic voltammograms and open-circuit potentiograms indicated that they have similar formation behavior of Dy–Ni phases with slightly different over-

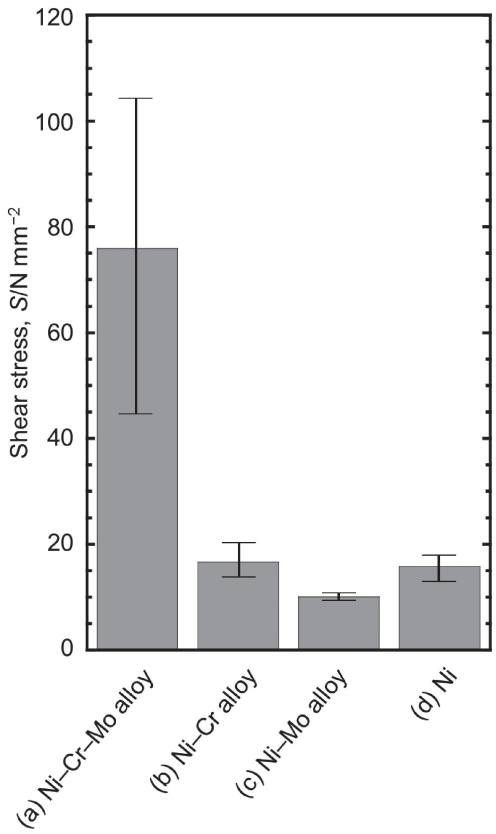

Fig. 8 Shear stress of the samples prepared by potentiostatic electrolysis of (a) Ni–Cr–Mo, (b) Ni–Cr, and (c) Ni–Mo plate electrodes at 0.20 V for 60 min in molten LiF–CaF_2–DyF_3 (0.30 mol%) at 1123 K. (d) The sample from the Ni plate was prepared at 0.20 V for 25–40 min in the same melt. Error bars represent their standard variations.

voltages. A Dy-alloyed sample having the $DyNi_2$ phase was prepared from each electrode by electrolysis at 0.20 V (vs. Li^+/Li) for 60 min. The SEM/TEM observation and EDX mapping analysis carried out on the sample from the Ni–Cr–Mo alloy, confirmed the phase separation into Dy–Ni–Fe matrix phase, Cr-rich Cr–Mo phase with a diameter of 0.2–1 µm, and Mo-rich Mo–Cr phase with a diameter of 50–100 nm. The results of the shear stress measurements clearly showed only Ni–Cr–Mo alloy exhibited the improvements in the mechanical strength of the alloys by precipitation strengthening, when compared with the result of Ni. Precipitation strengthening was not achieved by simple precipitation of the agglomerated phase, and the precipitation of both Cr–Mo and Mo–Cr phases are suggested to play important roles in increasing the mechanical strength. Because these Cr–Mo and Mo–Cr phases are supposed to be stable in the RE separation system, the durability of alloy diaphragm will be improved if Ni–Cr–Mo alloy is used as the starting material for the alloy diaphragm.

Acknowledgments

A part of this study was conducted as commission research with the New Energy and Industrial Technology Development Organization (NEDO).

REFERENCES

1) U.S. Geological Survey: Mineral Commodity Summaries 2020, (2020).
2) Y. Xu, L.S. Chumbley and F.C. Laabs: J. Mater. Res. **15** (2000) 2296–2304.
3) O. Takeda, T.H. Okabe and Y. Umetsu: J. Alloy. Compd. **379** (2004) 305–313.
4) S. Shirayama and T.H. Okabe: Molten Salts **52** (2009) 71–82 (in Japanese).
5) S. Shirayama and T.H. Okabe: Metall. Mater. Trans. B **49** (2018) 1067–1077.
6) O. Takeda, K. Nakano and Y. Sato: Molten Salts **52** (2009) 63–70.
7) H. Sekimoto, T. Kubo and K. Yamaguchi: J. MMIJ **130** (2014) 494–500 (in Japanese).
8) M. Matsumiya, H. Kondo, A. Kurachi, K. Tsunashima and S. Kodama: J. Japan Inst. Metals **75** (2011) 607–612.
9) T. Oishi, H. Konishi and T. Nohira: Japanese Patent (2014) JP 5504515.
10) T. Uda, K.T. Jacob and M. Hirasawa: Science **289** (2000) 2326–2329.
11) T. Oishi, H. Konishi, T. Nohira, M. Tanaka and T. Usui: Kagaku Kogaku Ronbunshu **36** (2010) 299–303 (in Japanese).
12) T. Nohira, S. Kobayashi, K. Kobayashi, R. Hagiwara, T. Oishi and H. Konishi: ECS Trans. **33** (2010) 205–212.
13) S. Kobayashi, K. Kobayashi, T. Nohira, R. Hagiwara, T. Oishi and H. Konishi: J. Electrochem. Soc. **158** (2011) E142–E146.
14) S. Kobayashi, T. Nohira, K. Kobayashi, K. Yasuda, R. Hagiwara, T. Oishi and H. Konishi: J. Electrochem. Soc. **159** (2012) E193–E197.
15) K. Yasuda, S. Kobayashi, T. Nohira and R. Hagiwara: Electrochim. Acta **92** (2013) 349–355.
16) K. Yasuda, S. Kobayashi, T. Nohira and R. Hagiwara: Electrochim. Acta **106** (2013) 293–300.
17) K. Yasuda, K. Kondo, T. Nohira and R. Hagiwara: J. Electrochem. Soc. **161** (2014) D3097–D3104.
18) K. Yasuda, K. Kondo, S. Kobayashi, T. Nohira and R. Hagiwara: J. Electrochem. Soc. **163** (2016) D140–D145.
19) Y. Watanabe, Y. Norikawa, K. Yasuda and T. Nohira: Mater. Trans. **60** (2019) 379–385.
20) K. Maeda, K. Yasuda, T. Nohira, R. Hagiwara and T. Homma: J. Electrochem. Soc. **162** (2015) D444–D448.
21) Y.Y. Pan and P. Nash: *Phase Diagrams of Binary Nickel Alloys*, ed. by P. Nash, (ASM International, Materials Park, 1991) p. 96.
22) T.B. Massalski, H. Okamoto, P.R. Subramanian and L. Kacprzak: *Binary Alloy Phase Diagrams*, 2nd ed., CD-ROM version 1.0, (1990).
23) P.E.A. Turchi, L. Kaufman and Z.-K. Liu: Calphad **30** (2006) 70–87.
24) M. Venkatraman and J.P. Neumann: Bull. Alloy Phase Diagrams **8** (1987) 289–290.
25) H. Okamoto: *Phase Diagrams of Binary Iron Alloys*, ed. by H. Okamoto, (ASM International, Materials Park, 1993) pp. 341–349.